A Composite Photocatalyst Based on Hydrothermally-Synthesized Cu_2ZnSnS_4 Powders

Shih-Jen Lin [1], Jyh-Ming Ting [1,*], Kuo-Chin Hsu [2] and Yaw-Shyan Fu [2,*] [ID]

[1] Department of Materials Science and Engineering, National Cheng Kung University, Tainan 701, Taiwan; andy.sjlin@gmail.com
[2] Department of Greenergy, National University of Tainan, Tainan 701, Taiwan; kuochin1225@gmail.com
* Correspondence: jting@mail.ncku.edu.tw (J.-M.T.); ysfu@mail.nutn.edu.tw (Y.-S.F.); Tel.: +886-6-260-5031 (Y.-S.F.); Fax: +886-6-260-2205 (Y.-S.F.)

Abstract: A novel composite photocatalyst based on Cu_2ZnSnS_4 (CZTS) powders was synthesized and investigated for use as a photocatalyst. CZTS powders were first made using a conventional hydrothermal method and were then used to grow silver nanoparticles hybridized onto the CZTS under various conditions through a microwave-assisted hydrothermal process. After the obtained samples were subsequently mixed with 1T-2H MoS_2, the three synthesized component samples were characterized using X-ray diffractometry (XRD), scanning electron microscopy, transmission electron microscopy (FE-SEM, FE-TEM), UV-visible spectroscopy (UV-Vis), Brunauer-Emmet-Teller (BET), photoluminescence spectroscopy (PL), and X-ray photoelectron spectroscopy (XPS). The resulting samples were also used as photocatalysts for the degradation of methylene blue (MB) under a 300 W halogen lamp simulating sunlight with ~5% UV light. The photodegradation ability was greatly enhanced by the addition of Ag and 1T-2H MoS_2. Excellent photodegradation of MB was obtained under visible light. The effects of material characteristics on the photodegradation were investigated and discussed.

Keywords: Cu_2ZnSnS_4 powders; silver nanoparticles; 1T-2H MoS_2; photodegradation

1. Introduction

A photocatalytic technique is considered a promising method for treating organic dyes in wastewater [1,2]. I_2-II-IV-VI_4 quaternary chalcogenide semiconductors Cu_2ZnSnS_4 (CZTS) are non-toxic, Earth-abundant, and inexpensive, and they have a high absorption coefficient $>10^{-4}$ cm^2 for potential application as solar-cell absorbers [3–5]. However, due to the fact that their optimum band gap is ~1.5 eV, they easily recombine into photogenerated holes and electrons. Thus, it is necessary to reduce the recombination rate. TiO_2 is a well-known n-type metal oxide photocatalyst in many photocatalytic applications, including hydrogen generation and water splitting in environmental and energy-related fields [1,6–9]. However, its relatively large band gap of 3.2 eV is only a small fraction (4%) of the solar spectrum. Several studies have investigated ways to achieve better absorption and charge carrier mobility under visible light through the use of a dopant [10–13]. Koichi Awazu et al. labeled this new phenomenon "plasmonic photocatalysis", where silver (Ag) nanoparticles (NPs) are coated with a passive material such as SiO_2 to prevent oxidation and to separate TiO_2. Their work indicated effective surface plasmon resonance transfer of photogenerated holes on the surface enhanced photocatalytic reaction [14].

Recently, it has been shown that silver orthophosphate (Ag_3PO_4) has extremely high photo-oxidative capabilities for O_2 generation from water splitting under visible light irradiation [15]. GO–Ag_3PO_4 nanocomposites have been synthesized as an excellent hybrid photocatalyst [16,17].

They not only exhibit enhanced visible light photocatalytic activity, but also show better stability and durability than their counterparts. Among them, molybdenum disulfide (MoS_2) exhibits a graphene-like layered structure in which S–Mo–S covalent bonds exist within the plane, and van der Waals forces hold the plane [2,18]. MoS_2 provides a high surface area, unique electrical conductivity consisting of 1T-2H hybridized phases, and a sheet-like morphology [19]. It has received attention for application in energy storage devices due to its unique nanostructure and electronic properties.

The photocatalysts of the I_2-II-IV-VI_4 quaternary group exhibit better absorption ability under visible light than TiO_2. Therefore, Xuelian Yu et al. prepared CZTS-Pt and CZTS-Au heterostructured NPs using a synthesis route [20]. The results showed enhanced photocatalytic activity toward photodegradation and hydrogen generation by water splitting. Feng Jiang et al. reported a multilayer of $Pt/In_2S_3/CdS/CZTS$ heterostrucures, where the obtained photocathode showed significant enhancement in terms of stability during photoirradiation for PEC water splitting [21]. Hybridized 1T-2H MoS_2 was then added to provide higher electrical conductivity and the specific surface area necessary to achieve superior catalytic ability [22–24]. Importantly, Ag was added in the structure to extend the light absorption of the photocatalyst to the visible light region, which was due to the surface plasmon resonance of Ag NPs, which enabled the photocatalyst to absorb light in the visible spectrum. Owing to these outstanding characteristics, we report a novel design of three-component Ag/hybridized CZTS/1T-2H MoS_2 heterojunction photocatalysts using a facile hydrothermal method. Since their appropriate band gap structures and stability enhance properties that include light harvesting, charge separation, and transfer photoactivity, it is essential to develop this method on a photocatalytic mechanism.

2. Results and Discussion

2.1. Crystal Structure

The XRD patterns of the Kesterite (KS) CZTS, 1T-2H MoS_2, and 1 wt% Ag-CZTS/1T-2H MoS_2 are shown in Figure 1. Figure 1a shows that the major CZTS diffraction peaks observed at 28.47°, 32.99°, 47.35°, 56.14°, 68.99°, and 76.42° can be indexed to the crystal planes of (112), (200), (220), (312), (008), and (332) of the KS structure (JCPDS no. 26-0575), respectively. The formation mechanisms of the CZTS powder are summarized as $Cu_2S + SnS_2 + ZnS \rightarrow Cu_2ZnSnS_4$. It is necessary for the excess thiourea concentration to be a homogeneous solution in order to effectively induce a self-assembly reaction through the conventional hydrothermal (CHT) method [4]. No secondary phases of Cu_2S, SnS_2 or ZnS were detected [25]. Figure 1b shows that the CHT synthesized MoS_2 microflower sample obtained the major diffraction peaks at 14.42°, 32.69°, 33.49°, 39.52°, 49.76°, and 58.3°, which correspond to the (002), (100), (101), (103), (105), and (110) crystalline planes of MoS_2 (JCPDS no. 37-1492), respectively. In addition, the calculated interlayer spacing (d-002) using the Bragg equation was 0.66 nm, with the reported well-controlled expansion of the interlayer d-spacing in the hydrothermal/solvothermal approaches ranging from 0.62 to 1.1 nm [26]. In Figure 1c for the 1 wt% Ag/CZTS and 2:1 ratio of 1T-2H MoS_2 composite, no peaks were observed for Ag probably due to the very small amount of Ag added onto the CZTS. The XRD pattern corresponding to both the CZTS and MoS_2 peaks can be observed.
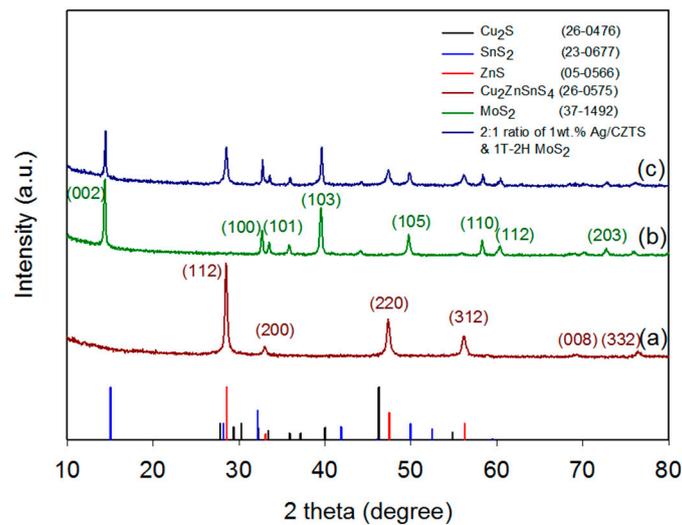
Figure 1. XRD pattern of (**a**) CZTS powders using the conventional hydrothermal process (CHT) at 180 °C for 72 h; (**b**) MoS$_2$ powder using the CHT process at 200 °C for 24 h; (**c**) 2:1 ratio of 1 wt% Ag/CZTS and 1T-2H MoS$_2$.

2.2. Morphology

The morphology of Ag/CZTS/1T-2H MoS$_2$ NPs based on the SEM results is shown in Figure 2. Figure 2a shows the SEM images of 1 wt% Ag hybridized KS CZTS NPs. Shapes with a minor amount of irregular particles were obtained, but the addition of Ag on the CZTS was not observed on the SEM images probably because the Ag particles were too small to be detected. Figure 2b shows the images of CHT-synthesized MoS$_2$ microflowers obtained as the petals, which consist of several MoS$_2$ nanosheets. On the other hand, Figure 2c shows that the morphologies of the as-prepared 2:1 ratio of 1 wt% Ag/CZTS and 1T-2H MoS$_2$ are well grown on the surface of the MoS$_2$ powder, thereby successfully forming the Ag/CZTS/1T-2H MoS$_2$ heterostructure.
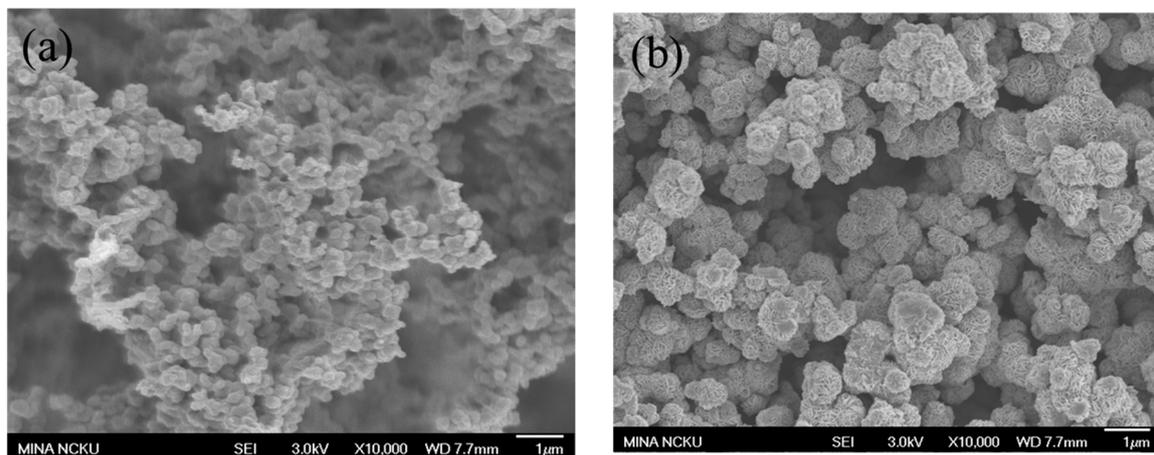
Figure 2. *Cont.*
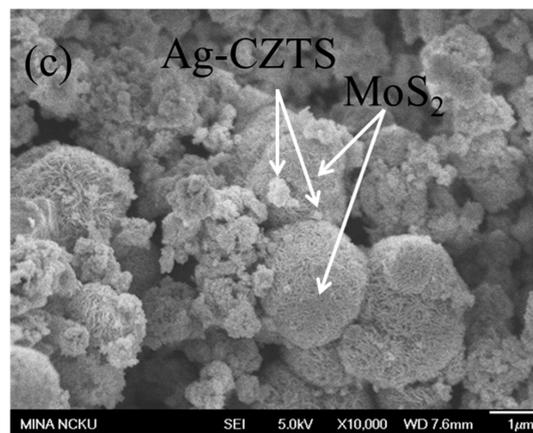
Figure 2. Scanning electron microscopy (SEM) images of the prepared CZTS powders with the (**a**) 1 wt% Ag doped on CZTS powder; (**b**) 1T-2H MoS_2 microflower; and (**c**) the 2:1 ratio of 1 wt% Ag/CZTS and 1T-2H MoS_2.

Figure 3a shows the TEM images of Ag/CZTS powders, where the Ag NPs with a darker contrast were hybridized on the CZTS powder. Figure 3d shows the high resolution TEM images wherein the interplannar lattice spacing of 0.31 nm corresponds to the (112) planes [5]. Meanwhile, the additional Ag corresponds to the face-centered cubic (FCC) Ag (111) [27], with a spacing of 0.24 nm. Figure 3b,e show that the microflower morphologies of MoS_2 consist of a considerable number of single and few layer structures. The MoS_2 lattice fringe spacing was also calculated, for which the corresponding d-spacing was 0.67 nm [22]. Figure 3c,f show the more aggregated nanoparticles of the 1 wt% Ag/CZTS and 2:1 ratio of 1T-2H MoS_2 and the SAED image of the 1 wt% Ag/CZTS and 2:1 ratio of 1T-2H MoS_2, which is consistent of with tetragonal KS CZTS, as it shows the major phases (112), (220), and (312), indicating that the hybridizing of the Ag NPs can be attributed to the diffraction from the (111) plane of FCC. The corresponding SAED results for the 1T-2H MoS_2 microflower match the (002), (100), and (110) planes [23,24].
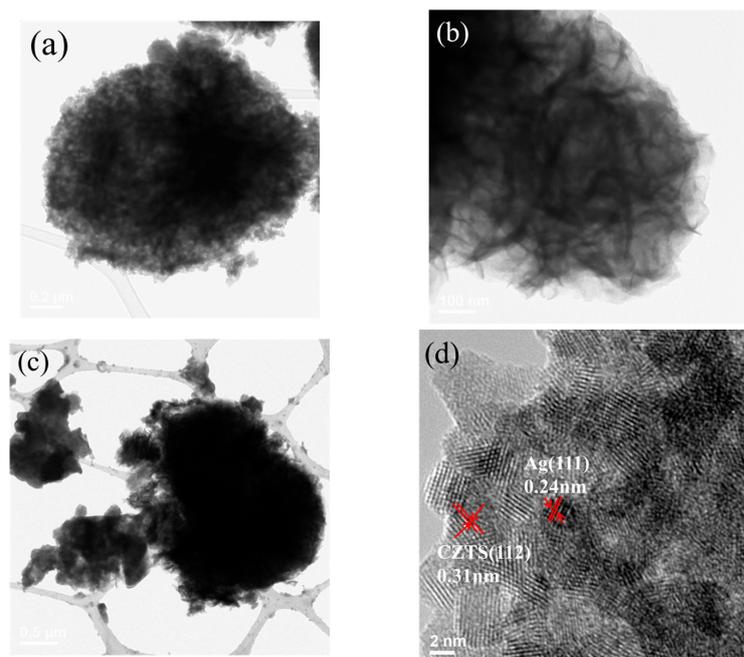
Figure 3. *Cont.*
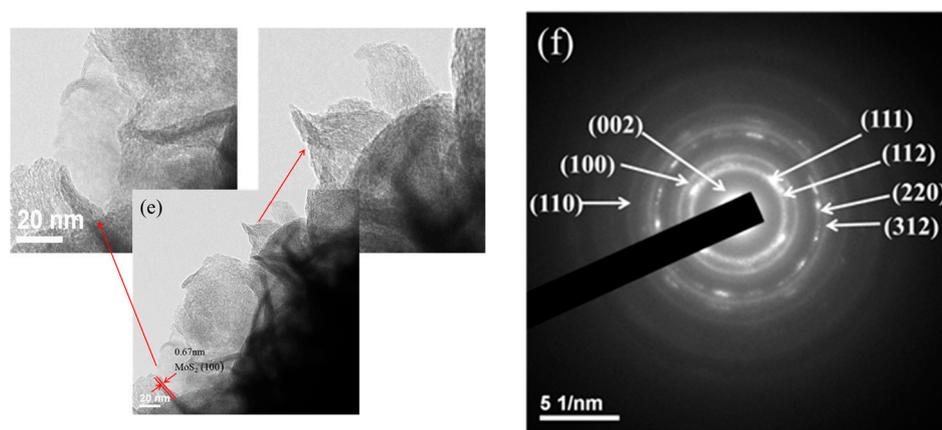
Figure 3. TEM images (**a**) 1 wt% Ag doped on CZTS powders; (**b**) 1T-2H MoS$_2$ microflower; (**c**) 2:1 ratio of 1 wt% Ag/CZTS and 1T-2H MoS$_2$; HRTEM images of (**d**) 1 wt% Ag/CZTS; (**e**) 1T-2H MoS$_2$ microflower; and (**f**) SAED micrographs of 2:1 ratio of 1 wt% Ag/CZTS and 1T-2H MoS$_2$.

2.3. Surface Areas

Figure 4 shows the Brunauer–Emmett–Teller (BET) analysis using N$_2$ adsorption-desorption isotherms and the corresponding Barrett–Joyner–Halenda (BJH) pore size distributions curves (inset). The surface areas of the CZTS powders and 1T-2H MoS$_2$ are measured as 3.38 and 21.39 m^2 g^{-1}, respectively. The insets are the BJH pore volume are 0.045 and 0.096 cm^3 g^{-1}, and the pore size distribution plot, for which the adsorption average pore diameters are 31.74 and 18.02 nm, respectively. It can be seen that there are differences in the morphology results in different specific surface areas (SSAs), which indicates that the MoS$_2$ has a higher SSA than is the case for the CZTS powders due to the fact that the microflower shape provided a higher surface area. However, the pore size of the 1T-2H MoS$_2$ is smaller than that of the CZTS powders. This may be because the alkaline solution of diethylenediamine (DETA) acted as an etchant and increased the excess thiourea, which is an intermolecular force and polarity molecule during the synthesis of the CZTS powders, resulting in the formation of more pits on the surface [28,29]. Therefore, the larger SSA and pore diameter in the Ag/CZTS/MoS$_2$ contributed to active enhancement of photo-catalytic efficiency [24].
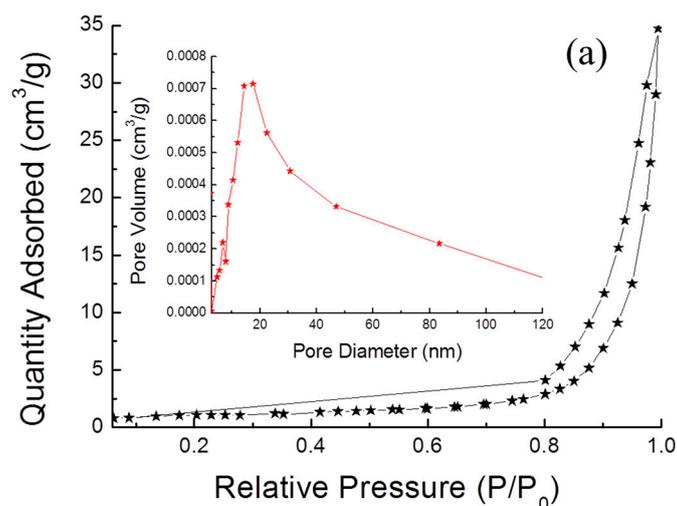
Figure 4. *Cont.*
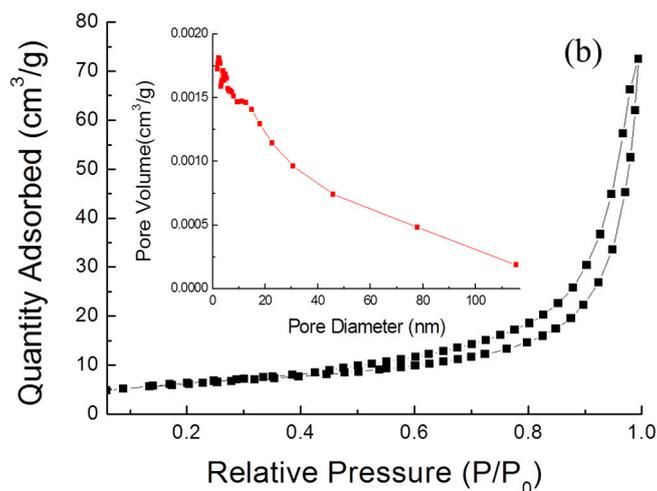
Figure 4. N_2 absorption/desorption isotherms of (**a**) CZTS powders, and (**b**) 1T-2H MoS_2 microflower powders; insets are BJH pore size distribution plots, respectively.

2.4. Optical Absorption

The UV-VIS absorption spectrum results for the tetragonal KS CZTS powders, 1 wt% Ag/CZTS, 1 wt% Ag/CZTS, and 10:1 and 2:1 ratios of 1T-2H MoS_2 are shown in Figure 5. It can be seen that doping Ag enhanced the light absorption, and this fact can be ascribed to the charge transfer process from the valence band to the conduction band by board surface plasmon resonance (SPR) absorption in the visible region [30]. However, further increases in the 10 wt% and 50 wt% 1T-2H MoS_2 microflower powder resulted in broad absorption due to a higher SSA. It is apparent that a high surface area enhances the visible light absorption. This is likely due to the strong monotonic absorption in the visible light region of the hybridized 1T-2H MoS_2. Among the samples, the 2:1 ratio of 1 wt% Ag/CZTS and 1T-2H MoS_2 exhibited the best enhancement.
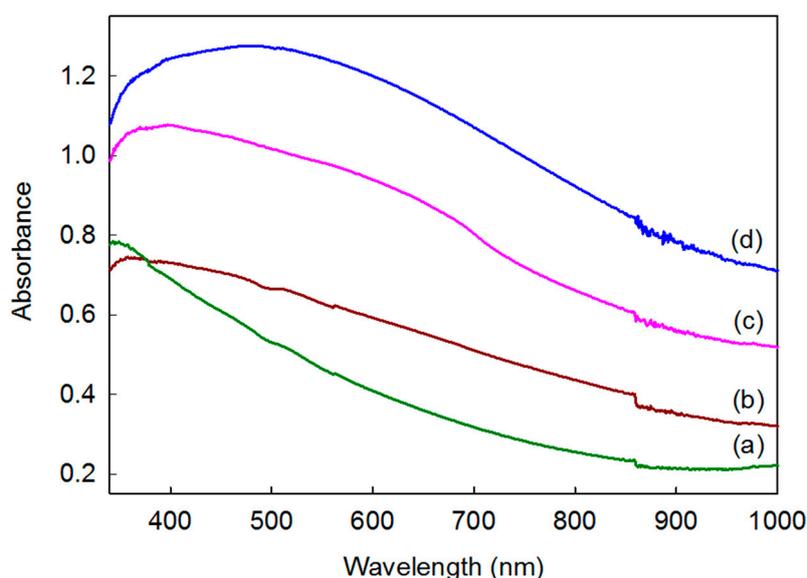
Figure 5. UV-VIS absorption spectra of (**a**) CZTS; (**b**) 1 wt% Ag/CZTS; (**c**) 10:1 ratio of 1 wt% Ag/CZTS and 1T-2H MoS_2; and (**d**) 2:1 ratio of 1 wt% Ag/CZTS and 1T-2H MoS_2.

2.5. PL Analysis

A PL analysis was then performed to determine the effect of Ag on the recombination rate of the photocatalyst. Figure 6 shows that the PL intensity was greatly increased when a 4 and 8 wt% of Ag was added to the CZTS photocatalyst, and a further decrease was observed when the amount was decreased to 2 and 1 wt%. This suggested that the electrons promoted in the conduction band of CZTS jump to the surface plasmon state of Ag, thus reducing the recombination rate of the structure. However, excessive amounts of electrons were generated in the structure, which caused the Ag nanoparticles to serve as a recombination site in the system [30]. On the other hand, 1 wt% Ag/CZTS hybridized a higher SSA of MoS_2 that absorbed the visible light and efficiently transferred the photogenerated charge carriers. The CZTS nanoparticles generated excited electrons and holes from its valence band to its conduction band after which the electrons generated in the CZTS conduction band jumped to the surface plasmon state of the Ag nanoparticles to be either directly transferred to MoS_2 or shuttled across the Ag to the MoS_2. Finally, the presence of hybridized Ag and 1T-2H MoS_2 microflower powders might indicate a decrease in the recombination rate necessary for photocatalysis.
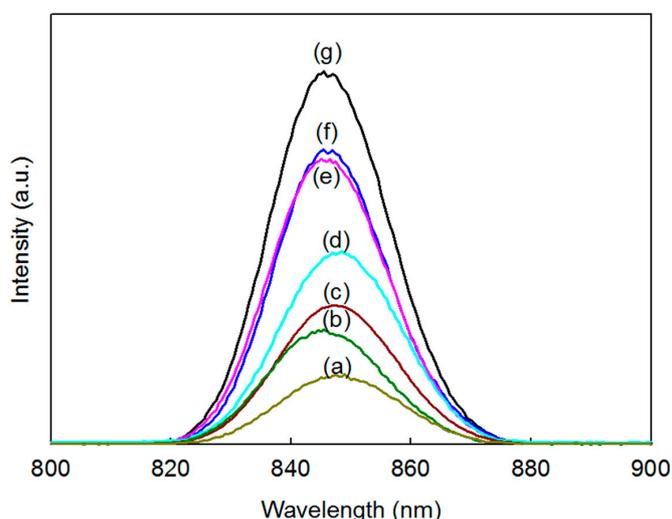
Figure 6. PL spectra of (**a**) 2:1 ratio of 1 wt% Ag/CZTS and 1T-2H MoS_2; (**b**) 10:1 ratio of 1 wt% Ag/CZTS and 1T-2H MoS_2; (**c**) 1 wt% Ag/CZTS; (**d**) 2 wt% Ag/CZTS; (**e**) CZTS; (**f**) 4 wt% Ag/CZTS; and (**g**) 8 wt% Ag/CZTS.

2.6. XPS Study

A calibration was made for each sample with respect to 284.6 eV of carbon C 1s. The XPS analysis carried out on the four constituent elements, copper 2p, zinc 2p, tin 3d, and sulfur 2p. (Figure 7a), showed the binding energy of the Cu $2p_{3/2}$ and Cu $2p_{1/2}$ peaks at 931.4 and 952.2 eV, respectively, with a peak splitting at 19.8 eV, suggesting Cu (I). Figure 7b showed the Zn $2p_{3/2}$ and Zn $2p_{1/2}$ peaks at 1021.8 and 1044.8 eV, respectively, with a peak splitting at 23 eV, corresponding to Zn (II). Figure 7c shows the Sn $3d_{5/2}$ and Sn $3d_{3/2}$ peaks at 485.8 and 494.2 eV, respectively, with peak splitting at 8.4 eV, which is in a good agreement with Sn (IV). Figure 7d shows the S $2p_{3/2}$, S $2p_{1/2}$ peaks at 161.1, 162.3 eV, respectively, from S (II) [5]. The Ag 3d XPS spectra of Ag/CZTS samples obtained from different weight percentages of $AgNO_3$ precursor: 1, 2, 4, and 8 wt% are shown in Figure 7e. The high resolution spectra of the Ag 3d core level for the samples showed two peaks, which were located around 368.2 eV and 374.3 eV. These peaks proved that $AgNO_3$ was successfully reduced to metallic Ag through the microwave-assisted hydrothermal process in water as a solvent [31]. Further confirmation of the existence of the hybridized 1T-2H phase of MoS_2 is provided in Figure 7f, where a typical MoS_2 microflower shows Mo $3d_{5/2}$ and Mo $3d_{3/2}$ peaks at 229.7 eV and 232.7 eV for the 2H phase, respectively, and an S 2s peak at 226.6 eV in the high resolution Mo 3d spectrum. Furthermore, a minor

peak at 235.7 eV appears to the Mo^{6+} $3d_{5/2}$. However, the samples shift toward lower energy peaks at 228.7 and 231.9 eV for the 1T phase, which shifts toward a lower binding energy with a difference of ~0.8 eV with respect to the peaks in the 1T-2H phase [18,19]. Similarly, Figure 7g shows the S 2p XPS spectra of the MoS_2 samples indicating that two additional signatures at 161.7 eV and 162.8 eV appear beside the two S $2p_{3/2}$ and S $2p_{1/2}$ 2H MoS_2 peaks at 162.6 eV and 163.7 eV, respectively. These two peaks also shift to the lower binding energy side and are associated with the 1T phase [19].
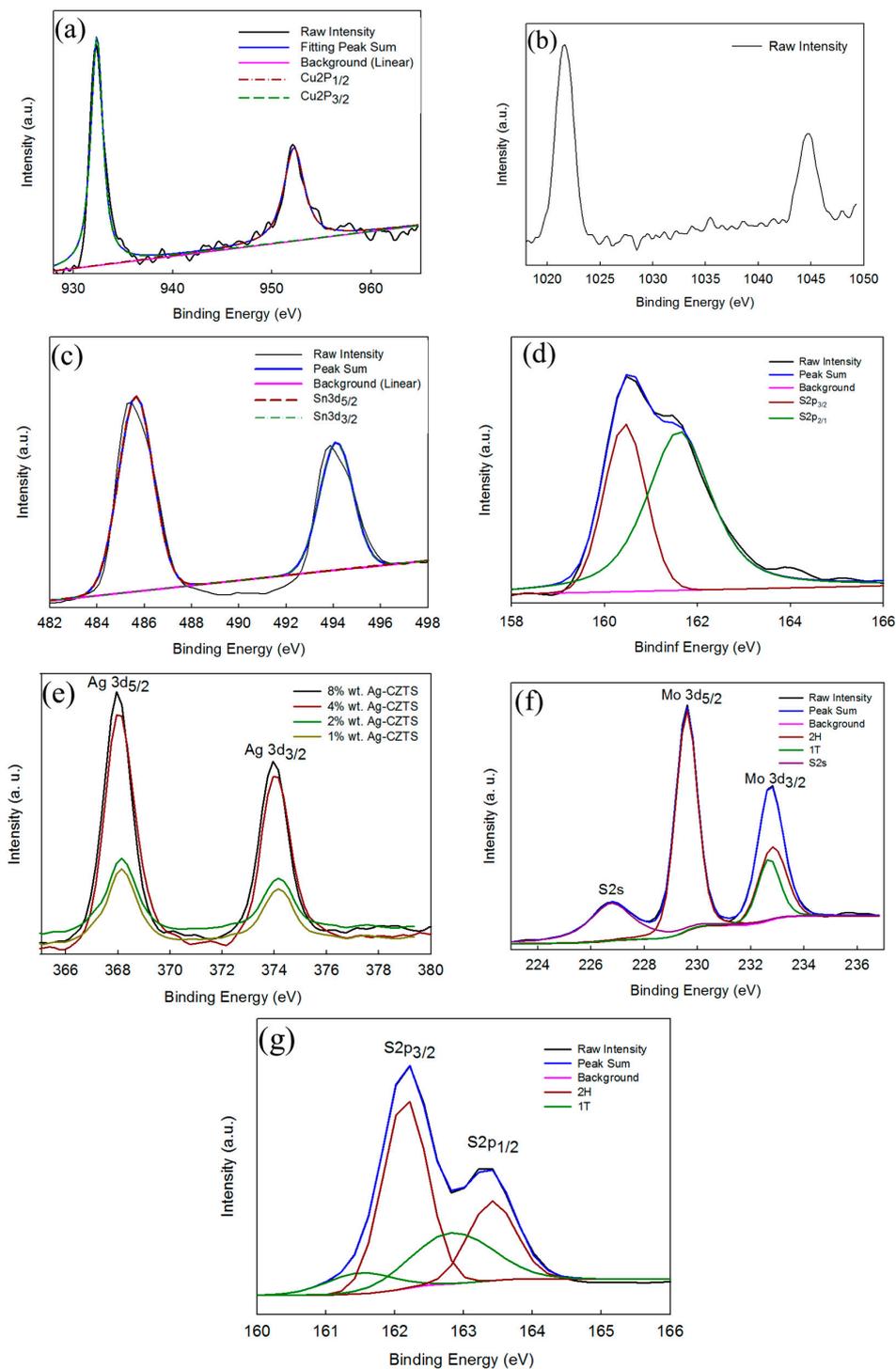
Figure 7. High-resolution XPS characterization of as-synthesized (**a**) Cu 2p; (**b**) Zn 2p; (**c**) Sn 3d; (**d**) S 2p; (**e**) Ag NPs; (**f**) Mo 3d; and (**g**) S 2p.

2.7. Photocatalytic Activity

The photocatalytic performance of all of the Ag/CZTS and hybridized 1T-2H MoS$_2$ photocatalysts were measured and compared with the photocatalytic performance. The curves of C/C$_0$, where C$_0$ is the initial concentration of MB, and C is the reaction concentration of MB at time t are shown in Figure 8a. It can be seen that the hybridized Ag decreased as the Ag content increased. In the case of the addition of 1T-2H MoS$_2$, regardless of whether the ratio was lower (10 wt%) or was 1 wt%, Ag doped on the CZTS greatly enhanced the photocatalytic performance. Figure 8b shows the first order linear transform, which was determined by plotting –ln (C/Co) versus irradiation time. The corresponding k values for the CZTS, 1, 2, 4, 8 wt% Ag, the 1 wt% Ag/CZTS, and the 10:1 and 2:1 ratios of the 1T-2H MoS$_2$ microflower powders samples were estimated to be 0.0025, 0.0039, 0.0033, 0.0024, 0.0019, 0.016, and 0.0213 min^{-1}, respectively. The photodegradation rate constant of the three component Ag/CZTS/1T-2H MoS$_2$ sample was faster than that for the CZTS and Ag/CZTS samples. A schematic diagram of the proposed mechanism is provided in Figure 9. The results were attributed to the combined effects of enhanced visible light absorption by Ag and the efficient charge separation due to the MoS$_2$ in the photocatalyst system. Due to the surface plasmon resonance, electrons below the Fermi level of the Ag nanoparticles excited to their plasmonic state. Then, the electrons generated in the CZTS conduction band jumped to the surface plasmon state of the Ag nanoparticles, thus reducing the recombination rate. The electrons generated in and transferred to the Ag nanoparticles reacted to O$_2$ gas to form superoxide radicals ($^{\bullet}O_2^{-}$). These active radicals reacted with the methylene blue solution to degrade it into H$_2$O and CO$_2$. On the other hand, the holes generated in the system reacted with the adsorbed H$_2$O to form hydroxyl radicals ($^{\bullet}OH$). These active radicals also reacted with the methylene blue solution to degrade it into H$_2$O and CO$_2$.
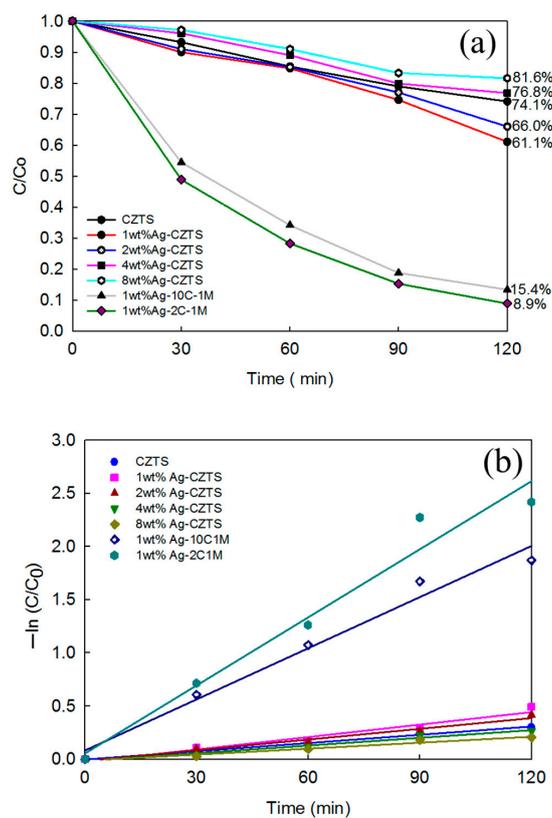
Figure 8. Photocatalytic activity under solar irradiation through the hybridized various weight percentages of AgNO$_3$ precursor: 1, 2, 4, and 8 wt% Ag/CZTS and the ratios of 10:1 and 2:1 of 1 wt% Ag/CZTS and 1T-2H MoS$_2$; (**a**) the degradation of MB; and (**b**) the photocatalytic degradation kinetics evolution.
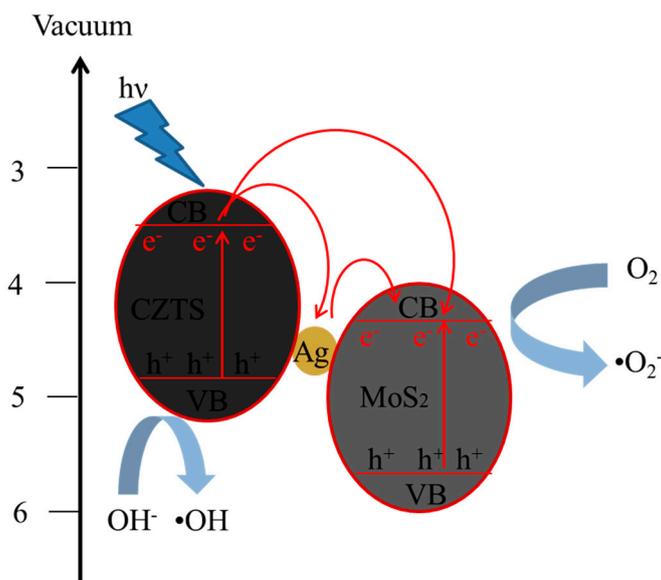
Figure 9. Schematic diagram for proposed photodegradation mechanism of methylene blue solution in the presence of the Ag/CZTS hybridized 1T-2H MoS$_2$ photocatalyst.

3. Materials and Characterization

3.1. Materials

All chemicals were used as received without further purification. Analytical grade materials included copper (II) chloride anhydrous (CuCl$_2$, Choneye pure chemicals Co., Ltd., Taipei City, Taiwan, 98%), zinc chloride (ZnCl$_2$, Merck, Kenilworth, NJ, USA, 98%), stannous chloride dehydrate (SnCl$_2$·2H$_2$O, Shimakyu, Osaka, Japan, 98%), thiourea (NH$_2$CSNH$_2$, Riedel-de Haën, Mexico City, Mexico, 99%), diethylenediamine (C$_4$H$_{13}$N$_3$, Panerac quimica sa, Barcelona, Spain, 98%), silver nitrate (AgNO$_3$, Aencore, Surrey Hills, Australia, 99.8%), sodium molybdate dihydrate (NaMoO$_4$·2H$_2$O, J.T. Baker, Center Valley, PA, USA, 99.5%), and oxalic acid (Riedel-de Haën, 99.5%), and the deionized water (DI water) used was from EMD Millipore Corporation.

3.2. CZTS Convental Hydrothermal Process

Deionized water was used as the solvent. In a typical aqueous synthesis, 30 mmol of thiourea was dissolved in 20 mL of deionized water in a 50 mL Teflon-lined autoclave and stirred for 15 min. 2.5 mmol of ZnCl$_2$ and SnCl$_2$·2H$_2$O were dissolved in 5 mL of deionized water, and 5 mmol of CuCl$_2$ (anhydrous) was used in 10 mL of deionized water. All of the precursors were stirred for 10 min individually and were then poured into the 50 mL Teflon-lined stainless-steel autoclave, with the addition 0.543 mL diethylenediamine (DETA) as the chelating agent. The autoclave was sealed and maintained at 180 °C for 72 h and then allowed to cool down to room temperature naturally. After hydrothermal synthesis, the solution was washed and centrifuged with dimethylformamide and deionized water three times to remove the byproducts and DETA. Black particles were then obtained by drying in an oven at 80 °C for 8 h.

3.3. Ag/CZTS Microwave-Assisted Hydrothermal Process

The obtained CZTS powers were charged 0.75 g then various amounts of AgNO$_3$ solution were added (1 wt%, 2 wt%, 4 wt%, and 8 wt% in 20 mL deionized water). The solution was then loaded into a Teflon-lined autoclave at 200 °C for 1 h in a microwave-assisted system for the hydrothermal process. Finally, the products were washed three times with ethanol and DI water, centrifuged, and dried overnight in a vacuum oven at 60 °C to obtain the 1, 2, 4, and 8 wt% Ag/CZTS powders.

3.4. MoS₂ Conventional Hydrothermal Process

MoS$_2$ synthesized from 5 mmol NaMoO$_4$·2H$_2$O and 5 mmol oxalic acid were dissolved in 20 mL DI water and then stirred for 20 min. Then, 20 mmol thiourea was added and dissolved in 10 mL DI water separately. The solutions were then loaded into a 50 mL Teflon-lined autoclave for the hydrothermal process at 200 °C for 24 h. The MoS$_2$ powders were then collected and washed three times with ethanol and DI water. They were then dried at 60 °C overnight in a vacuum oven.

3.5. Ag/CZTS/MoS₂ Hybridized Process

Finally, three components of the Ag/CZTS/MoS$_2$ composite were mixed in 20 mL of ethanol with the varying weight ratios of 1 wt% Ag/CZTS and MoS$_2$ powder 10:1 and 2:1 for 1 h. The products were washed three times with DI water and ethanol and then dried at 60 °C overnight in a vacuum oven.

3.6. Characterization

The crystalline structure of the powders was examined using X-ray diffraction (XRD Bruker D8 advance, Billerica, MA, USA). The morphology was determined using field emission scanning electron microscopy (FESEM, JEOL JSM-6701F, Tokyo, Japan). The microstructure was investigated using transmission electron microscopy (TEM, JEOL JEM-2100F, Tokyo, Japan). X-ray photoelectron spectroscopy (XPS, ULVAC-PHI, Inc. PHI 5000 VersaProbe, Chigasaki-shi, Japan) spectra were obtained using a 1486.6 eV Al anode X-ray source. XPS peak 4.1 software was used for the peak fitting, where the resulting peak components were pure Gaussian. The surface area was measured according to Brunauer-Emmet-Teller (BET, Micromeritics Instrument Corp. Tristar II, Norcross, GA, USA). The optical properties of particle suspensions were determined using a UV-VIS absorption spectrum (PerkinElmer Lambda 7500, Waltham, MA, USA). The PL spectra were obtained using a LS-55 fluorescence spectrometer (PerkinElmer, Waltham, MA, USA).

3.7. Photocatalytic Behavior

Methylene blue (MB), which is widely utilized in organic dye textile industries, is typically used in photocatalytic dye degradation studies. All the samples were carried out using 20 mg of the photocatalysts in 60 mL of 20 ppm methylene blue solution. The solution was stirred in the dark for 30 min to achieve the adsorption-desorption equilibrium. Furthermore, stirring was continued under a 300 W halogen lamp intended to simulate sunlight with ~5% UV light. Then, ~4 mL of the charged solution was collected every 30 min and centrifuged for 15 min to remove the photocatalyst completely. The concentration of MB solution was measured with the absorbance at 664 nm with the UV–VIS spectrophotometer (PerkinElmer Lambda 7500, Waltham, MA, USA).

4. Conclusions

In this paper, we discuss the use of a conventional hydrothermal method for the synthesis of Cu$_2$ZnSnS$_4$ powders well indexed into a high-purity KS phase. Furthermore, hybridized Ag/CZTS was successfully synthesized through a microwave-assisted hydrothermal process using water as the solvent for such processes as ultrasound and microwave irradiation to facilitate chemical reactions. It was found that the photocatalytic performance of the CZTS powders was greatly improved by the addition 1 and 2 wt% of Ag NPs deposited on the surface of the CZTS acting as the electron traps of the matrix. This prevented the recombination of electron-hole pairs and improved the charge transfer processes by hybridizing the 1T-2H MoS$_2$ in the structure, thus increasing the light harvesting in photocatalysis due to the broad light absorption range. This technique was attributed to the strong enhancement of visible light absorption and efficient charge separation, leading to reduced recombination. A maximum of 91.1% MB degradation occurred in under 2 h, where the photocatalyst containing a 2:1 ratio of 1 wt% Ag/CZTS and 1T-2H MoS$_2$ exhibited the highest photodegradation.

Author Contributions: All of the authors contributed to this work, discussed the results and implications, and commented on the manuscript. Jyh-Ming Ting conceived the strategies and designed the experiments. Shih-Jen Lin performed the experiments and wrote the paper. Kuo-Chin Hsu assisted with the analytical tools. Yaw-Shyan Fu reviewed and contributed to the final manuscript.

Conflicts of Interest: The authors declare no conflict of interest.

References

1. Ratna; Padhi, B.S. Pollution due to synthetic dyes toxicity & carcinogenicity studies and remediation. *Int. J. Environ. Sci.* **2012**, *3*, 940–955. [CrossRef]

2. Kochuveedu, S.T.; Jang, Y.H.; Kim, D.H. A study on the mechanism for the interaction of light. *Chem. Soc. Rev.* **2013**, *42*, 8467–8493. [CrossRef] [PubMed]

3. ITO, K.; Nakazawa, T. Electrical and optical properties of sannite-type quaternary semiconductor thin film. *Jpn. J. Appl. Phys.* **1988**, *11*, 2094–2097. [CrossRef]

4. Katagiri, H.; Jimbo, K.; Maw, W.S.; Oishi, K.; Yamazaki, M.; Araki, H.; Takeuchi, A. Development of CZTS-based thin film solar cells. *Thin Solid Films* **2009**, *517*, 2455–2460. [CrossRef]

5. Riha, S.C.; Parkinson, B.A.; Prieto, A.L. Solution-based synthesis and characterization of Cu_2ZnSnS_4 Nanocrystals. *J. Am. Chem. Soc.* **2009**, *131*, 12054–12055. [CrossRef] [PubMed]

6. Akpan, U.G.; Hameed, B.H. Parameters affecting the photocatalytic degradation of dyes using TiO_2-based photocatalysts: A review. *J. Hazard. Mater.* **2009**, *170*, 520–529. [CrossRef] [PubMed]

7. Pelaez, M.; Nolan, N.T.; Pillai, S.C.; Seery, M.K.; Falaras, P.; Kontos, A.G.; Dunlop, S.M.; Hamilton, J.W.; Byrne, J.A.; O'Shea, K.; et al. A review on the visible light active titanium dioxide photocatalysts for environmental applications. *Appl. Catal. B Environ.* **2012**, *125*, 331–349. [CrossRef]

8. Gaya, U.I.; Abdullah, A.H. Heterogeneous photocatalytic degradation of organic contaminants over titanium dioxide: A review of fundamentals, progress and problems. *J. Photochem. Photobiol. A Rev.* **2008**, *9*, 1–12. [CrossRef]

9. Kumar, A.; Mathur, N. Photocatalytic degradation of aniline at the interface of TiO_2 suspensions containing carbonate ions. *J. Colloid Interface Sci.* **2006**, *300*, 244–252. [CrossRef] [PubMed]

10. Asahi, R.; Morikawa, T.; Ohwaki, T.; Aoki, K.; Taga, Y. Visible-Light Photocatalysis in Nitrogen-Doped Titanium Oxides. *Science* **2001**, *293*, 269–271. [CrossRef] [PubMed]

11. Sathish, M.; Viswanathan, B.; Viswanath, R.P.; Gopinath, C.S. Synthesis, characterization, electronic structure, and photocatalytic activity of nitrogen-Doped TiO_2 nanocatalyst. *Chem. Mater.* **2005**, *17*, 6349–6353. [CrossRef]

12. Chen, X.; Burda, C. The electronic origin of the visible-light absorption properties of C-, N- and S-doped TiO_2 nanomaterials. *J. Am. Chem. Soc.* **2008**, *130*, 5018–5019. [CrossRef] [PubMed]

13. Williams, G.; Seger, B.; Kamat, P.V. TiO_2-graphene nanocomposites uv-assisted photocatalytic reduction of graphene oxide. *Am. Chem. Soc. Nano* **2008**, *7*, 1487–1491. [CrossRef] [PubMed]

14. Awazu, K.; Fujimaki, M.; Rockstuhl, C.; Tominaga, J.; Murakami, H.; Ohki, Y.; Yoshida, N.; Watanabe, T. A plasmonic photocatalyst consisting of silver nanoparticles embedded in titanium dioxide. *J. Am. Chem. Soc.* **2008**, *130*, 1676–1680. [CrossRef] [PubMed]

15. Yi, Z.; Ye, J.; Kikugaw, N.; Kako, T.; Ouyang, S.; Stuart-Williams, H.; Cao, J.; Luo, W.; Li, Z.; Liu, Y.; et al. An orthophosphate semiconductor with photooxidation properties under visible-light irradiation. *Nat. Mater.* **2010**, *9*, 559–564. [CrossRef] [PubMed]

16. Yang, X.; Cui, H.; Li, Y.; Qin, J.; Zhang, R.; Tang, H. Fabrication of Ag_3PO_4-Graphene composites with highly efficient and stable visible light photocatalytic performance. *ACS Catal.* **2013**, *3*. [CrossRef]

17. Liang, Q.; Shi, Y.; Ma, W.; Li, Z.; Yang, X. Enhanced photocatalytic activity and structural stability by hybridizing Ag_3PO_4 nanospheres with graphene oxide sheets. *Phys. Chem. Chem. Phys.* **2012**, *14*, 15657–15665. [CrossRef] [PubMed]

18. Geng, X.; Sun, W.; Wu, W.; Chen, B.; Al-Hilo, A.; Benamara, M.; Zhu, H.; Watanabe, F.; Cui, J.; Chen, T.P. Pure and stable metallic phase molybdenum disulfide nanosheets for hydrogen evolution reaction. *Nat. Commun.* **2016**, *7*, 1–7. [CrossRef] [PubMed]

19. Jiang, L.; Zhang, S.; Kulinich, S.A.; Song, X.; Zhu, J.; Wang, X.; Zeng, H. Optimizing hybridization of 1t and 2h phases in mos$_2$ monolayers to improve capacitances of supercapacitors. *Mater. Res. Lett.* **2015**, *3*, 177–183. [CrossRef]

20. Yu, X.; Shavel, A.; An, X.; Luo, Z.; Ibáñez, M.; Cabot, A. Cu$_2$ZnSnS$_4$-Pt and Cu$_2$ZnSnS$_4$-Au heterostructured nanoparticles for photocatalytic water splitting and pollutant degradation. *J. Am. Chem. Soc.* **2014**, *130*, 9236–9239. [CrossRef] [PubMed]

21. Jiang, F.; Gunawan; Harada, T.; Kuang, Y.; Minegishi, T.; Domen, K.; Ikeda, S. Pt/In$_2$S$_3$/CdS/Cu$_2$ZnSnS$_4$ thin film as an efficient and stable photocathode for water reduction under sunlight radiation. *J. Am. Chem. Soc.* **2015**, *137*, 13691–13697. [CrossRef] [PubMed]

22. Xia, Y.; Wanga, B.; Zhaoa, X.; Wang, G.; Wang, H. Core-shell composite of hierarchical MoS$_2$ nanosheets supported on graphitized hollow carbon microspheres for high performance lithium-ion batteries. *Electrochim. Acta* **2016**, *187*, 55–64. [CrossRef]

23. Ha, E.; Liu, W.; Wang, L.; Man, H.W.; Hu, L.; Tsang, E.S.C.; Chan, C.T.L.; Kwok, W.M.; Lee, L.Y.S.; Wong, K.Y. Cu$_2$ZnSnS$_4$/MoS$_2$-Reduced graphene oxide heterostructure: Nanoscale interfacial contact and enhanced photocatalytic hydrogen generation. *Sci. Rep.* **2017**, *7*, 1–8. [CrossRef] [PubMed]

24. Gogoi, G.; Arora, S.; Vinothkumar, N.; De, M.; Qureshi, M. Quaternary semiconductor Cu$_2$ZnSnS$_4$ loaded with MoS$_2$ as a co-catalyst for enhanced photo-catalytic activity. *R. Soc. Chem.* **2015**, *5*, 40475–40783. [CrossRef]

25. Turnbull, M.J.; Khoshmashrab, S.; Wang, Z.; Harbottle, R.; Sham, T.K.; Ding, Z. Controlling Cu$_2$ZnSnS$_4$ photocatalytic ability through alterationsin sulfur availability. *Catal. Today* **2016**, *260*, 119–125. [CrossRef]

26. Rasamani, K.D.; Alimohammadi, F.; Sun, Y. Interlayer-expanded MoS$_2$. *Mater. Today* **2017**, *20*, 83–91. [CrossRef]

27. Wang, X.; Tang, Y.; Chen, Z.; Lim, T.T. Highly stable heterostructured Ag–AgBr/TiO$_2$ composite: A bifunctional visible-light active photocatalyst for destruction of ibuprofen and bacteria. *J. Mater. Chem.* **2012**, *22*, 23149–23158. [CrossRef]

28. Mackinnon, D.J.; Brannen, J.M.; Morrison, R.M. The effect of thiourea on zinc electrowinning from industrial acid sulphate electrolyte. *J. Appl. Electrochem.* **1988**, *18*, 252–256. [CrossRef]

29. Cheong, W.J.; Luan, B.L.; Shoesmith, D.W. The effects of stabilizers on the bath stability of electroless Ni deposition and the deposit. *Appl. Surf. Sci.* **2004**, *229*, 282–300. [CrossRef]

30. Pugazhenthiran, N.; Murugesan, S.; Anandan, S. High surface area Ag-TiO$_2$ nanotubes for solar/visible-light photocatalytic degradation of ceftiofur sodium. *J. Hazard. Mater.* **2013**, *263*, 541–549. [CrossRef] [PubMed]

31. Dallinger, D.; Kappe, C.O. Microwave-Assisted Synthesis in Water as Solvent. *Chem. Rev.* **2007**, *107*, 2563–2591. [CrossRef] [PubMed]